

# Rapid crystallization of the Animikie Red Ace Pegmatite, Florence county, northeastern Wisconsin: inclusion microthermometry and conductive-cooling modeling

Mona-Liza C. Sirbescu · Emily E. Hartwick · James J. Student

Received: 17 August 2007 / Accepted: 11 February 2008 / Published online: 4 March 2008  
© Springer-Verlag 2008

**Abstract** We evaluated the crystallization regime of a zoned pegmatite dike and the degree of magma undercooling at the onset of crystallization by analyzing coeval fluid and melt inclusion assemblages. The liquidus temperature of the pegmatite magma was  $\sim 720^{\circ}\text{C}$ , based on re-melting of crystallized-melt inclusions in heating experiments. The magma crystallized sequentially starting with a thin border zone, which formed in less than one day at an average temperature of  $\sim 480^{\circ}\text{C}$  based on primary fluid inclusions, meaning  $240^{\circ}\text{C}$  undercooling. The primary inclusions from the outer zones were postdated by secondary inclusions trapped between  $580$  and  $720^{\circ}\text{C}$ , representing fluid exsolved from hotter, still crystallizing inner pegmatite units. The huge temperature contrast between the pegmatite's inner and outer zones was simulated by conductive-heat numerical modeling. A  $2.5$  m wide dike emplaced in  $220^{\circ}\text{C}$  rocks cools entirely to  $<400^{\circ}\text{C}$  in less than 50 days. Unidirectional and skeletal textures also indicate rapid, disequilibrium crystallization.

**Keywords** Fluid inclusion assemblages · Melt inclusion assemblages · Microthermometry · LCT pegmatite · Numerical simulation · Undercooling ·

Disequilibrium crystallization · Florence county pegmatite field · Wisconsin

## Introduction

Rare-element granitic pegmatites are magmatic intrusive bodies formed by water-rich silicate melts enriched in elements such as Li, Rb, Cs, B, P, and F. The continuing quest for a better understanding of granitic pegmatite petrogenesis stems from their frequent occurrence in convergent orogens, important role in mass-redistribution of light elements (Li, B, P, F), LILE's, and other incompatible elements, and their economic significance. A revitalized interest for rare element pegmatites is due to their resources of tantalum and niobium as strategic metals and gemstones (Ercit et al. 2003; Marshall et al. 2004).

Widely-accepted petrogenetic models do not offer a comprehensive explanation of the exotic mineralogy, extreme range of textures and crystal sizes, and internal zoning of pegmatites (Černý et al. 2005; London 2005), mainly because the parental materials, the phase relations, and physical conditions during melt generation, emplacement, and crystallization are poorly constrained. Field studies of several pegmatites that belong to the lithium–cesium–tantalum (LCT) type of Černý (1993a) suggest unusually low temperatures of magmatic crystallization, ranging from  $\sim 450^{\circ}\text{C}$  to as low as  $350^{\circ}\text{C}$  (Morgan and London 1999; Sirbescu and Nabelek 2003), which are  $200$ – $400^{\circ}\text{C}$  lower than the wet haplogranitic solidus (Luth et al. 1964). These occurrences were attributed to high degrees of melt undercooling and/or the cumulative depolymerizing effect that multiple fluxing components have on the melt structure (Thomas et al. 2000; Sirbescu and Nabelek 2003; London 2005; Černý et al. 2005 and references therein).

Communicated by T. L. Grove.

M.-L. C. Sirbescu (✉) · E. E. Hartwick · J. J. Student  
Geology Department, Central Michigan University,  
314 Brooks Hall, Mount Pleasant, MI 48859, USA  
e-mail: sirbelmc@cmich.edu

### Present Address:

E. E. Hartwick  
Wolverine Gas and Oil Corporation, 1 Riverfront Plaza,  
55 Campau NW, Grand Rapids, MI 49503, USA

Regardless of the intrinsic cause of the crystallization-temperature depression, a minimum temperature at which melt may be present is constrained by the external temperature regime. Using conductive cooling modeling, Webber et al. (1999) estimated that the crystallization of ~1 m thick dikes lasts ~5 days and crystals grow with rates of  $\sim 5 \times 10^{-5}$  cm/s (4 cm/day) if temperature of the host rocks was ~150°C. Morgan and London (1999) attributed crystallization temperatures ranging from 435 to 375°C of such thin dikes to the high degrees of magma undercooling, suppressed nucleation rates, and increased diffusivities in the presence of fluxing components such as H<sub>2</sub>O, B, F, etc. Additionally, fluxes depress the glass transition temperature of aluminosilicate melts, as shown in experiments (Bouhfid et al. 2006). Therefore, fluxes (water in particular) permit the undercooled liquid to exist at these unusually low temperatures (Nabelek and Sirbescu 2006).

Fluid inclusion research on tourmaline-bearing miarolitic Transbaikalian pegmatites underscored the unusual enrichments of Na, B, ±F at the magmatic to hydrothermal transition, leading to appearance of an immiscible hydrosilicate “melt-like gel” (Touret et al. 2007 and references therein). In addition, the presence of an immiscible peralkaline hydrosilicate phase was noted in rare-metal peraluminous pegmatites (Thomas et al. 2005) as well as in experiments in the system Na<sub>2</sub>O–B<sub>2</sub>O<sub>3</sub>–SiO<sub>2</sub>–H<sub>2</sub>O (Smirnov et al. 2005) and hydrous peraluminous granite spiked with a few weight percent each of P<sub>2</sub>O<sub>5</sub>, B<sub>2</sub>O<sub>3</sub>, F, Rb, Cs, and Li (Veksler and Thomas 2002). These studies indicate that immiscibility may play an important role in the late-stage crystallization paths of pegmatitic magmas, as documented in highly fractionated cores and miaroles.

We propose that disequilibrium, rapid crystallization at high degrees of undercooling of moderately fluxed melts may better account for reaching such extreme enrichments in zoned pegmatites, rather than traditional fractional crystallization models (e.g., Cameron et al. 1949). In this contribution, fluid and melt inclusion microthermometry and heat transfer numerical simulations bring evidence of rapid crystallization at high values of undercooling in thin pegmatite dikes. The intrinsic crystallization parameters are consistent with the pressure–temperature conditions inferred from independent studies.

## Geological setting

### The Penokean orogen

The Florence county pegmatite field is located in northeastern Wisconsin, ~15 km south of the border with northern Michigan (Fig. 1). The pegmatites intrude rocks of the 1,875–1,835 Ma Penokean orogen, ~1,400 km

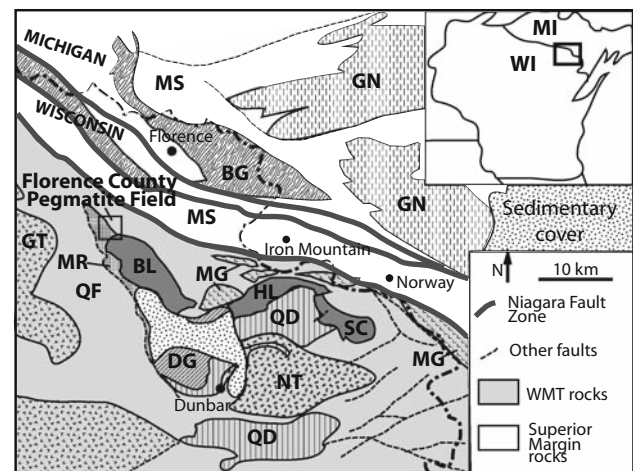


**Fig. 1** Geology of northeastern Wisconsin including the Florence county pegmatite field (after Sims et al. 1992). Superior Province Margin units: *MS* Michigamme Slate, *BG* Badwater Greenstone, *GN* Undifferentiated gneisses. Wisconsin Magmatic Terrane (*WMT*): Dunbar dome granitoids: *BL* Bush Lake Granite, *HL* Hoskin Lake Granite, *SC* Spike Creek Granite, *QD* Quartz diorite, *DG* Dunbar Gneiss; *GT* Undifferentiated granite and tonalite; and metamorphic units: *QF* Quinnesec Formation metavolcanics, *MR* Metasedimentary rocks, *MG* Metagabbro, and *NT* Newingham Tonalite

long belt of thrust-and-fold deformation, metamorphism, and magmatism formed during accretion and collision of the early proterozoic Wisconsin magmatic terrane (*WMT*) onto the southern margin of the Archean superior province (Van Schmus 1976; Schneider et al. 2002; Holm et al. 2005). The pegmatite field is situated ~5 km south of the steeply dipping Niagara fault zone (*NFZ*, Hoffman 1989). The *NFZ* marks the initially dextral-oblique, south-dipping subduction zone and ultimately the suture between (1) the *WMT* juvenile island-arc rocks, including synorogenic granitoids, metavolcanics, and sedimentary sequences and (2) the Superior province continental margin supracrustal rocks, here represented by bimodal metavolcanics and iron ranges, metasedimentary Michigamme formation, and Badwater metabasalts in part synchronous with the arc-related *WMT* (Schneider et al. 2002). A pulse of post-tectonic, undeformed granitoids with U-Pb zircon ages of ~1,835 Ma that intruded the *WMT* (Sims et al. 1985) was also documented north of *NFZ* (Schneider et al. 2002), thus, stitching the suture between the two blocks and marking the end of the Penokean deformation.

### Magmatism

Three episodes of granitic magmatism in northeastern Wisconsin area are pertinent to this study: (1) a syntectonic pulse that occurred ~1,860 Ma, (2) a late pulse ~1,835 Ma, and (3) a post-Penokean pulse ~1,760 Ma.

Although not dated, the Florence county pegmatites appear to be late or to postdate the Penokean deformation. Late, undeformed pegmatites and aplitic dikes are adjacent to and in part crosscut syn- to late orogenic granitoids of the structure named the Dunbar dome (Sims et al. 1992; Fig. 1). The undeformed, peraluminous Bush Lake granite (Fig. 1; not dated) in the northwest lobe of the Dunbar dome is the most probable parental granitic magma for the pegmatites in the Florence county. This is based on pegmatite close proximity (<3 km) to outcrops of the Bush Lake granite and strong geochemical affinities (Sims and Van Schmus 1988; Koehler 1990; Sims et al. 1992). The Bush Lake granite grades from peraluminous biotite granite to pegmatitic leucogranite with accessory Mn-rich garnet, tourmaline, beryl, and muscovite (Koehler 1990). Its contacts with the country rocks are covered by glacial deposits, except for some crosscutting granite and pegmatite dikes extending west and north from the main body (Sims et al. 1992; Falster et al. 2001). It is possible that Bush Lake granite and the associated pegmatites may be part of a ~1,760 magmatic pulse related to the subducted slab rollback towards southeast and collapse of the overthickened Penokean crust (Holm et al. 2005). In northern Wisconsin, these post-tectonic granites were emplaced at relatively shallow depths of 10–11 km (Holm et al. 2005).

## Metamorphism of the country rocks

The country rocks hosting the Florence county pegmatites belong to the  $1,866 \pm 39$  Ma (U-Pb zircon age; Sims et al. 1992) Quinnesec formation (Dutton 1971), a supracrustal, early Penokean unit dominated by metavolcanic rocks regionally metamorphosed to greenschist and amphibolite facies (Sims et al. 1992). Minor metasedimentary layers include quartz–mica schists, iron formation, and quartzites (Dutton 1971). Andalusite and cordierite-bearing schists were reported (Geiger and Guidotti 1989; Falster et al. 1997), indicating Abukuma-type metamorphism of low to moderate pressure, the common emplacement environment for the class of rare-element pegmatites (Černý 1993b).

## The Animikie Red Ace Pegmatite

The Animikie Red Ace Pegmatite (ARA) is located in the Florence SE 7.5' USGS quadrangle, of northeastern Wisconsin (Dutton 1971). Coordinates for a prominent outcrop are N 45° 51' 1.5", W 88° 21' 9.8". The pegmatite was named by Falster and Simmons (1988) for the Animikie Series of Bayley et al. (1966) and because of the distinct raspberry-red tourmaline in its wall zone. The ARA is part of a field comprising >200 non-miarolitic

**Table 1** Minerals in the ARA pegmatite zones (modified after Falster et al. 1996)

	Maximum width (cm)	Major minerals	Minor minerals
<b>Pegmatite zones</b>			
Border (BZ)	0.3	Plagioclase, microcline, quartz, acicular-radiating tourmaline, wall zone tourmaline "roots"	Apatite, pyrochlore, columbite–tantalite, cassiterite
Wall (WZ)	10	Comb-textured tourmaline, muscovite, microcline, quartz	Manganoanfluorapatite, spessartine, rhodizite, pollucite, columbite–tantalite, tantite, wodginite
Outer intermediate (IZ1)	100	Microcline, quartz	Tourmaline, lepidolite, columbite–tantalite
Middle intermediate (IZ2)	25	Tourmaline, phosphate nodules	Manganoanfluorapatite/apatite/lithiophilite nodules
Inner intermediate (IZ3)	20	Albite, microcline, lepidolite, quartz	Tourmaline
Core (CZ)	50	Quartz, lepidolite, albite (only in the core margin), spodumene	Microcline and phosphates (only in the core margin), tourmaline, columbite–tantalite
<b>Other units</b>			
Albite–aplite units	10 × 70 <sup>a</sup>	Albite	Tourmaline, mangano–apatite, columbite–tantalite
Albite, lepidolite, or albite–lepidolite replacement units and stringers		Albite replacing IZ K-feldspar Lepidolite on fractures and/or replacing WZ and IZ tourmaline and CZ spodumene	Columbite–tantalite
Lepidolite foot-wall "line-rock" pods	20 × 1,200 <sup>a</sup>	Lepidolite, quartz, albite in alternating layers	Microlite

<sup>a</sup> Represent maximum width × length (cm)

pegmatite dikes, most <10 m long, in an area of ~25 km<sup>2</sup> in Florence county (Falster et al. 2001; Falster et al. 2005). Previously, this pegmatite field was referred to as the Hoskin Lake pegmatite field, alluding to the probable parental granite, but it is named here the Florence county pegmatite field to avoid the confusion existing in the literature between the Hoskin Lake and Bush Lake granites.

The ARA dike trends approximately NS, dipping 40 to 60°W. It is ~600 m long and ≤2.5 m wide, but it is covered by ~100 m swampy terrain along its strike. Where contacts are exposed, the ARA intrudes discordantly to sub-concordantly quartz–mica schists and amphibolites of the Quinnesec formation. A ~5 cm wide aureole of tourmalinization occurs along the pegmatite exo-contacts. Angular rafts of country rock included in the pegmatite are also tourmalinized.

According to the revised pegmatite classification of Černý and Ercit (2005), the ARA is a hybrid of the lepidolite and spodumene subtypes of the complex type, rare element–lithium subclass (REL–Li), because it contains abundant lepidolite, some beryl, and minor pollucite (lepidolite component) along with spodumene and minerals of the columbite–tantalite series (spodumene component). Falster et al. (1996) identified several distinct internal mineral zones and late crosscutting and replacing units (Table 1): (1) a 1–3 mm thin, border zone (BZ) containing fine-grained plagioclase, microcline, quartz, apatite, and roots of wall-zone tourmaline crystals; (2) 10–20 cm thick wall-zone (WZ) with coarse comb-textured tourmaline, quartz, muscovite, and microcline; also, in the footwall zone, <20 cm thick lepidolite pods with continuous “line-rock” structure can be followed along strike for <120 m; (3) an outer intermediate zone (IZ1), <1 m thick, with quartz and microcline, minor lepidolite, and minor tourmaline; (4) <25 cm thick, middle intermediate zone (IZ2) with abundant blue or pink tourmaline and phosphate nodules; (5) <20 cm thick inner intermediate zone (IZ3) with albite, microcline, lepidolite, and quartz, minor tourmaline; and (6) <55 cm thick core (CZ) dominated by quartz and spodumene and without feldspar except in ~5 cm of the core margin. A typical cross section through the ARA is not symmetrical (Fig. 2); the zones are discontinuous and their thickness and mineral assemblages vary greatly along strike. Later units include the following: an albite–aplite unit crosscutting the internal zones and albite, lepidolite, and albite–lepidolite stringers and replacement units affecting the main zones (Table 1). Samples were collected along the pegmatite’s strike at locations numbered starting with 406 and 325 in the southern portion of the dike and in the northern portion of the dike, respectively.

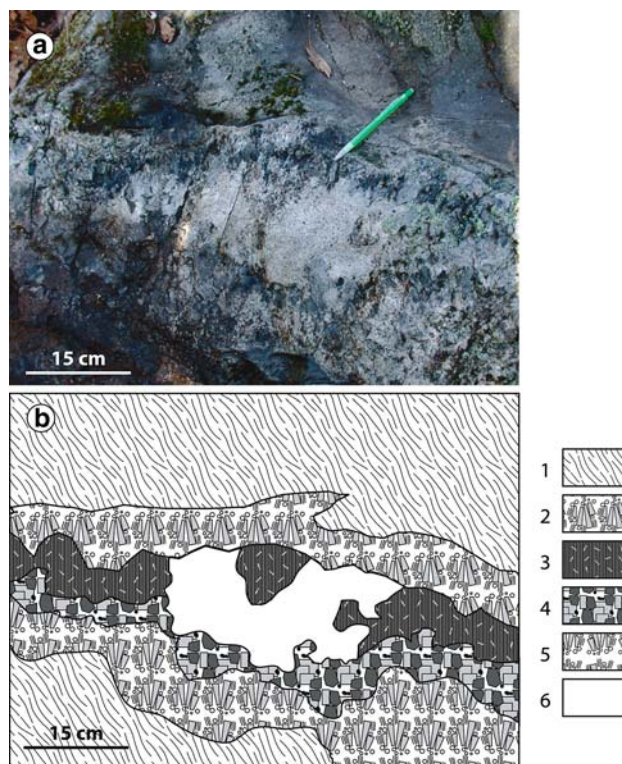


**Fig. 2** Cross-section through the ARA dike: **a** photograph and **b** interpretative sketch. Legend: **1** Biotite schist, **2** Hanging wall zone with comb-texture tourmaline, **3** Undifferentiated hanging wall intermediate zones ± core, **4** Footwall outer intermediate zone with massive dark gray quartz and K-feldspar, **5** Layered footwall zone with comb-texture tourmaline and late albite–lepidolite stringers, **6** Late albite–aplitic unit

## Methods

### Petrography and microthermometry

Fluid inclusion assemblages (FIAs) and melt inclusion assemblages (MIAs) in tourmaline, quartz, and apatite were mapped and described using a petrographic microscope and classified according to established textural and phase relations criteria (Roedder 1984; Goldstein and Reynolds 1994; Bodnar and Student 2006). Petrography was supplemented by cathodoluminescence imaging using an ELM-4 luminoscope. Freezing–heating measurements of fluid inclusions were performed between –195°C and 550°C on 150–300 μm thick, doubly-polished sections using a US Geological Survey (USGS)-type Fluid Inc. gas-flow stage calibrated with SynFlinc synthetic fluid inclusions, at –56.6, –21.2, 0.0, and 374.1°C. The phases observed during freezing and heating experiments were as follows: solid CO<sub>2</sub>, ice, clathrate (CO<sub>2</sub>·4.75 H<sub>2</sub>O), halite, other daughter minerals or incidentally trapped crystals, CO<sub>2</sub> liquid and vapor, and aqueous liquid and vapor. Inclusions with long dimension perpendicular to the

microscope stage were avoided to reduce the errors of the volumetric visual estimates.

Final homogenization temperatures were reproduced to  $\pm 2.0^\circ\text{C}$  and ice-melting, clathrate-dissolution, and  $\text{CO}_2$  homogenization temperatures were reproduced to  $\pm 0.3^\circ\text{C}$ . To improve accuracy, we used repeated warming and cooling cycles just below the expected phase change (Shepherd et al. 1985). Inclusions that stretched or leaked during the freezing/heating runs were discarded. The MacFlinCor program of Brown and Hagemann (1995) was used to estimate inclusion compositions and densities, and the inclusion isochores were calculated using appropriate equations of state (see below). Daughter minerals in inclusions exposed at the surface were identified on polished sections or freshly fractured samples by energy dispersive spectral (EDS) analysis on a JEOL 840A Scanning Electron Microscope.

#### Crystallized-melt inclusion microthermometry

Crystallized-melt inclusions decrepitated on a conventional USGS-type microthermometry stage at temperatures above  $400^\circ\text{C}$ . To prevent fluid loss, inclusion melting and quenching was carried in Holloway-type internally heated pressure vessels (IHPV). Chips of doubly polished sections containing well-documented inclusions were cut into  $\sim 2 \times 5\text{-mm}^2$  rectangles to be treated at temperatures ranging from  $550$  to  $720^\circ\text{C}$  and at pressures of 3–4 kbars. We used a stepwise approach. After each run, the changes were observed and documented on a Zeiss microscope with up to  $100\times$  magnification objective, equipped with a digital camera, and then heated again, until inclusions melted completely. In each experimental run, one to two chips were arranged between the ends of two inconel-sheathed, chromel–alumel thermocouples inside a copper cylinder to record temperatures and temperature gradients along the sample chips. An additional internal platinum tube was used to avoid direct contact between sample and the copper cylinder and to minimize the sample darkening. Both thermocouples were calibrated periodically against the freezing points of LiCl ( $605^\circ\text{C}$ ) and NaCl ( $800.5^\circ\text{C}$ ) and considered to be accurate to within  $2^\circ\text{C}$ . Temperature differences across the samples ranged from 0 to  $20^\circ\text{C}$ . Silica wool material was packed around the sample chips and the thermocouple to reduce the thermal gradients (Jenkins and Clare 1990). Pressures were monitored with a bourdon tube gauge accurate to  $\pm 50$  bar. To prevent inclusion recrystallization, cooling lasted only 4.5 minutes, with average quenching rates of  $\sim 300^\circ\text{C}/\text{min}$  from  $700$  to  $200^\circ\text{C}$ , and of  $\sim 67^\circ\text{C}/\text{min}$  from  $200$  to  $15^\circ\text{C}$ . In addition to microscopy, to validate that the remelted inclusions quenched to a homogeneous glass, some samples were repolished to expose inclusions at the surface and investigated using

backscatter electron imaging on a JEOL 8900 Superprobe electron microprobe at Binghamton University.

#### Petrography

Mineral textures in the BZ and WZ were studied, because they are pertinent to the onset of crystallization processes. In particular, we focused on tourmaline, apatite, and quartz as main host minerals for fluid and melt inclusions. We also studied textural evidence of early country-rock–pegmatite melt interaction and of internal deformation and metasomatic effects related to the crystallization of the ARA internal units.

#### Country rock

At the traverses sampled in this study, the ARA is in contact with a fine-grained quartz micaschist. Strongly pleochroic tourmaline replaces biotite of the country rock (CR; Fig. 3a, b). Tourmalinization decreases gradually and vanishes within  $<5$  cm from the sharp contact with the pegmatite. Other potentially metasomatic minerals identified within the first centimeters from the contact include microcline, apatite, calcite, pyrochlore, and cassiterite.

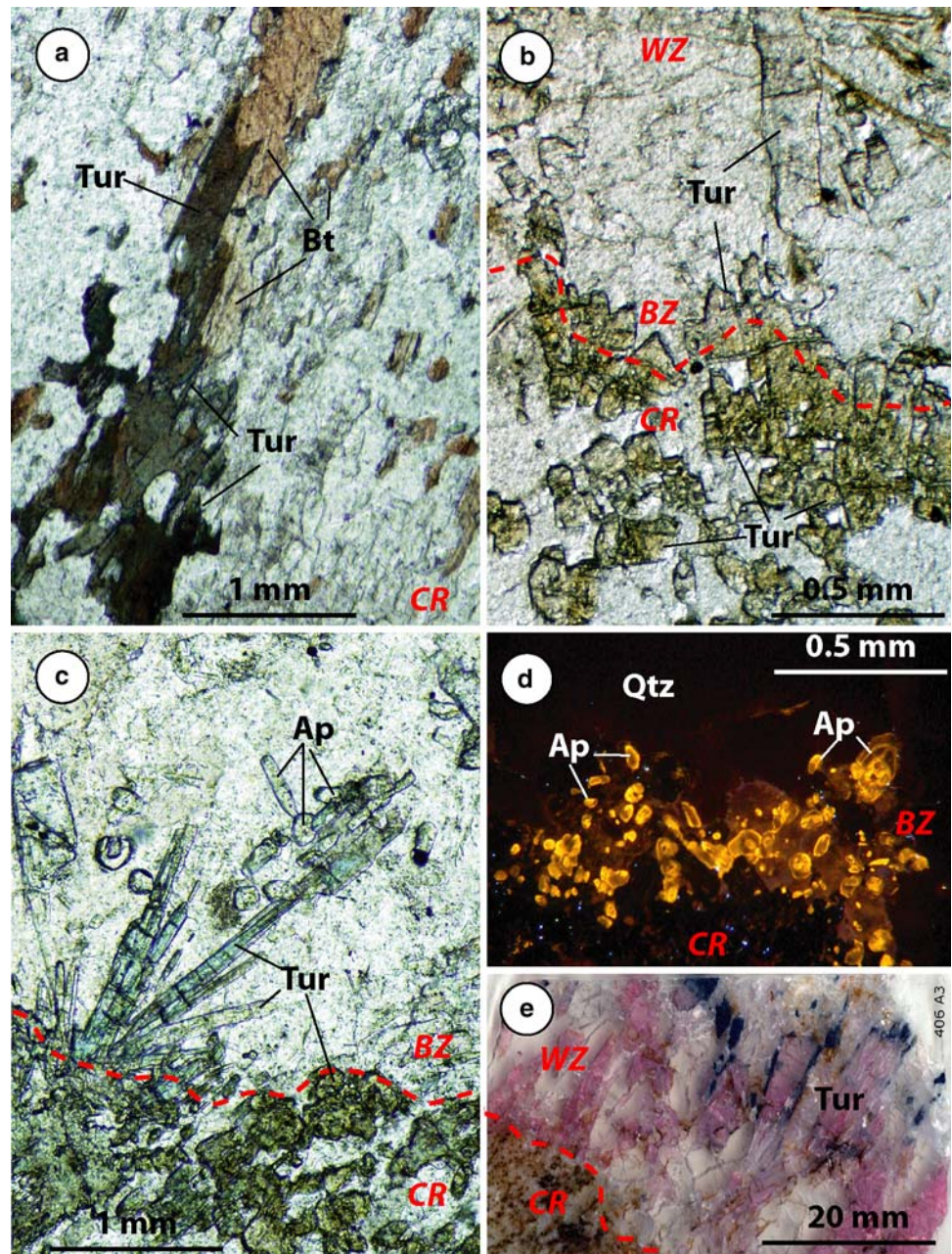
#### Border zone

A fine-grained,  $<3$  mm layer of quartz  $\pm$  K-feldspar  $\pm$  lepidolite, apatite, and tourmaline appears to constitute a chilled margin assemblage (Fig. 3c, d). Accessory phases of the border zone include pyrochlore and columbite-tantalite group minerals. Border zone (BZ) tourmaline occurs typically in acicular, radiating aggregates nucleating directly on the contact surface (Fig. 3c), especially when the contact is subconcordant to the foliation. In areas of highly discordant contacts, tourmaline crystals are in optical continuity with metasomatic tourmaline of the CR. The contact is marked by a change in color, from Mg–Fe-rich, intensely pleochroic green-brown tourmaline of the schist to Mg–Fe-poor, colorless or low pleochroic tourmaline of the pegmatite (Fig. 3b). BZ apatite occurs as  $<0.1$  mm ovoid, subhedral grains with abundant primary melt and a few fluid inclusions. The extremely rich abundance of zoned apatite is shown in the CL image (Fig. 3d).

#### Wall zone

Crystal sizes range from millimeters to a few centimeters. Comb textured,  $<5$  cm long, colored tourmaline is characteristic, although not in a continuous layer (Fig. 3e). Often, wall zone (WZ) tourmaline is zoned, with a core of pink elbaite (rubellite) and a rim of blue, Fe–Mn-rich tourmaline

**Fig. 3** Microphotographs. *Dashed line* is the country rock-pegmatite boundary. Abbreviations: *CR* country rock, *BZ* border zone, *WZ* wall zone, *Tur* tourmaline; *Ap* apatite, *Ab* albite, *Qtz* quartz, *Lpd* lepidolite, *Mt* muscovite, *Bt* biotite. **a** Partial tourmalinization of biotite in the *CR* at ~4 cm from the contact; **b** Change in tourmaline color marking a discordant contact between the *ARA* and *CR*; **c** Typical *BZ* assemblage with acicular tourmaline and ovoid to short prismatic apatite; **d** Cathodoluminescence image at the contact between *CR* and *ARA* with high nucleation of apatite in the *BZ*; **e** Thin section with pink-blue *WZ* tourmaline at contact with partially tourmalinized biotite schist; **f** *WZ* assemblage: skeletal tourmaline with lepidolite internal ring; **g** *WZ* assemblage: skeletal muscovite–quartz intergrowth and spherulitic muscovite crystals; **h** *WZ* assemblage affected by a late unit: tourmaline is replaced by lepidolite and quartz is deformed and recrystallized; **i** Late albite–lepidolite unit: myrmekite-like intergrowth seen perpendicular to (001) plane of mica; **j** Sharp contact between a late albite–lepidolite unit and *WZ* quartz; **k** Comb texture albite–lepidolite on the contact with *WZ* (*inset* from **j**)



of later generation (Fig. 3e). Most tourmaline crystals are skeletal, with internal rings or cores occupied by lepidolite or quartz or both (Fig. 3f). A uniaxial positive variety of manganofluorapatite occurs as subhedral, <5 mm long prisms, blue in hand sample, with numerous fluid and melt inclusions. Coarse myrmekite-like mica–quartz intergrowths and spherulitic mica aggregates also occur in the *WZ* (Fig. 3g).

#### Inner zones (intermediate zone and core zone)

The intermediate zone (*IZ*) and core zone (*CZ*) do not show a significant increase in crystal size when

compared to the *WZ*. Twenty- to thirty-centimeter large masses of anhedral dark quartz and partially albitized K-feldspar were the coarsest crystals recognized.

#### Late, crosscutting or replacement units

Late albitite, lepidolite, and albite–lepidolite masses or stringers affect to various degrees all pegmatite zones. Tourmaline is partially replaced by fine-grained mica, while quartz suffers fracturing and subgrain recrystallization (Fig. 3h). Large myrmekite-like mica–quartz intergrowths are frequent in the albite–lepidolite masses,

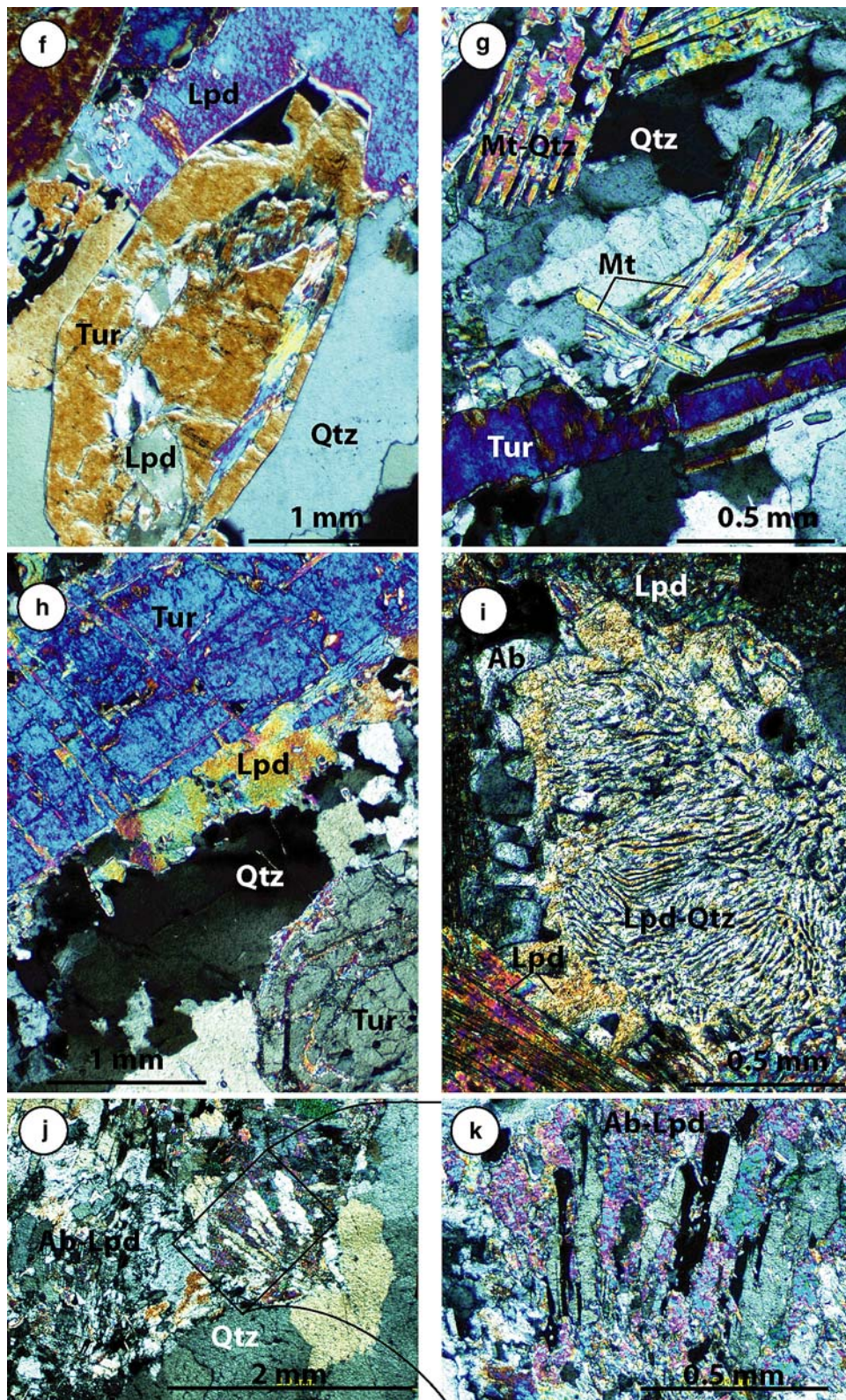


**Fig. 3** continued

suggesting rapid, concomitant crystallization of mica and quartz (Fig. 3i). The late units were deposited at least in part from a silicate liquid, as suggested by comb-

textured blue tourmaline and albite–lepidolite aggregates nucleated along sharp contacts on preexisting crystals (Fig. 3j, k).

## Fluid inclusions

### Primary fluid inclusions (type 1)

Eighty-one type 1 inclusions were analyzed in tourmaline (from BZ, WZ, and an albite–aplite unit sampled at ~20 cm from the contact), BZ apatite, and BZ quartz (Table 2). Crystals affected by replacement or fractures

were avoided. Most primary inclusions were ~5–45  $\mu\text{m}$  long, of tubular or subhedral shape, mimicking the crystal habit of the host tourmaline or apatite (Fig. 4a–c). The main criterion for establishing the primary character of inclusions in tourmaline was their shape and location within crystal growth zones (Roedder 1984). The primary character of inclusions in fine-grained BZ apatite and quartz, which lacked obvious growth-zones, was based on

**Table 2** Summary of ARA fluid inclusion results

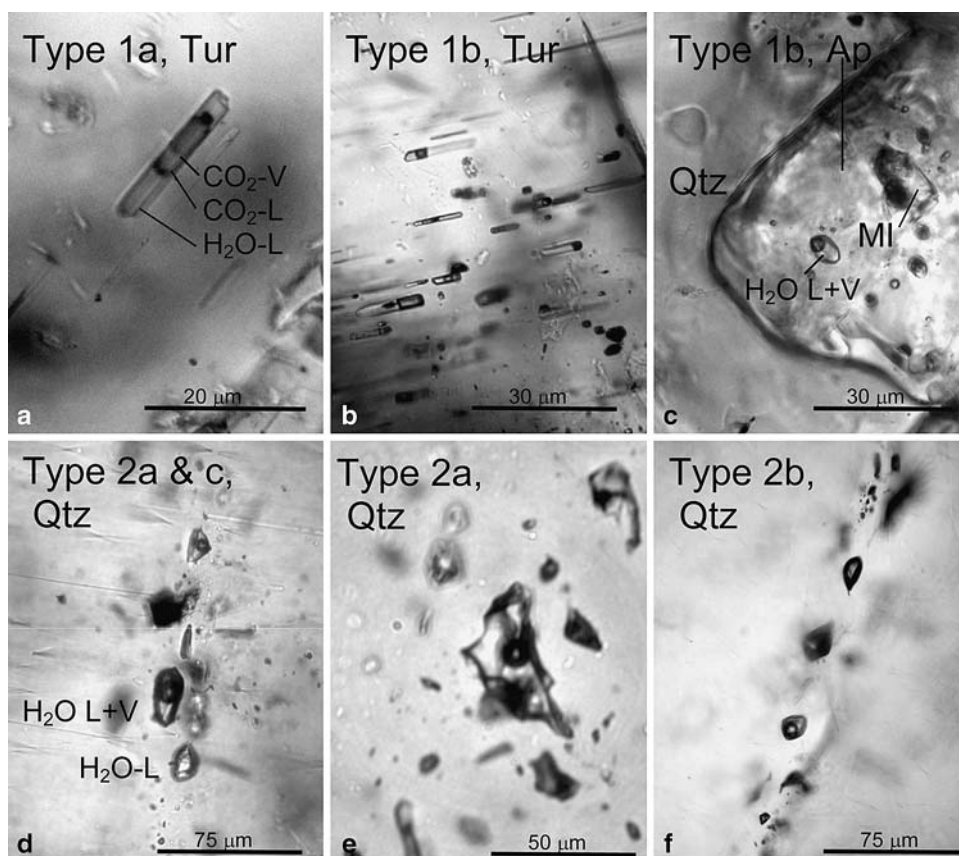
Sample				$T_h$ ( $^{\circ}\text{C}$ )	Weight percentage (wt%) of $\text{NaCl}_{\text{eq}}^a$	$T_{\text{mclath}}$ ( $^{\circ}\text{C}$ )	$X_{\text{CO}_2}$	$\rho$ ( $\text{g}/\text{cm}^3$ )
Locality	Number	Pegmatite zones	Host mineral					
ARA north	325G2	WZ	Pink <i>Tur</i>	303–330	4.2–6.4	6.6–7.8	0.07–0.16	0.84–0.92
	325G2-c	WZ	Pink <i>Tur</i>	304–340	6.4–10.0	4.3–6.6	0.08–0.16	0.76–0.88
ARA south	406A2	WZ, HW	Pink <i>Tur</i>	311–337	7.2–8.8	5.1–6.1	0.06–0.09	0.89–0.96
	406A2-a	WZ, HW	Pink/blue <i>Tur</i>	297–318	3.9–6.7	6.4–8.0	0.07–0.18	0.78–0.88
	406A2-b	WZ, HW	Pink/blue <i>Tur</i>	301–340	2.9–10.2	4.2–8.5	0.05–0.09	0.84–0.91
	406D-d	WZ, HW	Pink/blue, <i>Tur</i>	300–301	2.9–3.0	8.5–8.6	0.08	0.84–0.92
	406B2-b	Aplite unit	Blue <i>Tur</i>	301–326	4.3–7.9	5.7–7.8	0.12–0.23	0.73–0.78
Mean $\pm$ standard deviation, number of inclusions				315 $\pm$ 12, 36	6.2 $\pm$ 1.9, 34	6.7 $\pm$ 1.1, 34	0.1 $\pm$ 0.04, 36	0.86 $\pm$ 0.05, 36

Primary type 1a inclusions:  $\text{H}_2\text{O}-\text{CO}_2-\text{CH}_4-\text{NaCl}_{\text{eq}}$  system

ARA north the northern segment of the dike, ARA south the southern segment of the dike, HW hanging wall, WZ wall zone, *Tur* tourmaline

<sup>a</sup> Partial salinity of the aqueous portion of the mixed inclusions

**Fig. 4** ARA fluid inclusions. Abbreviations: *L* liquid; *V* vapor. **a, b** Type 1a  $\text{H}_2\text{O}-\text{CO}_2$  and type 1b aqueous inclusions in WZ tourmaline; **c** Type 1b and melt inclusion (*MI*) in BZ apatite surrounded by quartz; **d, e** Type 2a (two-phase) and 2c (one-phase) aqueous inclusions in WZ quartz; **f** Type 2b aqueous inclusions in WZ quartz; the one phase (*V*) inclusion appears to have decrepitated





inclusion distribution in three-dimensional arrays, with no apparent alignment on fractures (Fig. 4c). In addition, the magmatic character of type 1 fluids in tourmaline and apatite was validated by their coeval occurrence with melt inclusions (Fig. 4c).

Two compositional subtypes were separated. Type 1a inclusions, found only in tourmaline (Fig. 4a), are H<sub>2</sub>O–CO<sub>2</sub> mixtures with two or three phases at ~25°C: H<sub>2</sub>O liquid and CO<sub>2</sub> liquid ± gas. Type 1b inclusions found in tourmaline (Fig. 4b), apatite (Fig. 4c), and rarely in quartz are H<sub>2</sub>O solutions of variable salinity, with no detectable CO<sub>2</sub>.

Type 1a inclusions ( $N = 36$  inclusions from seven samples, Table 2) have narrow range of final melting point of CO<sub>2</sub> ( $T_{mCO_2}$ ) from –58.2 to –56.6°C, dissolution temperature of clathrate ( $T_{mclath}$ ) from 4.2 to 8.5°C, and homogenization temperatures ( $T_h$ ) from 297 to 340°C (Fig. 5). Homogenization occurred to a liquid phase. Molar fraction of methane ( $X_{CH_4}$ ) dissolved in the CO<sub>2</sub>-rich phase ranges from 0.02 to 0, based on  $T_{mCO_2}$  data, using Thiery et al. (1994). The bulk  $X_{CO_2}$  ranges from 0.046 to 0.232, and salinity of the aqueous portion of inclusions (NaCl<sub>eq</sub>) ranges from 2.9 to 10.2 wt% NaCl<sub>eq</sub> (Fig. 5) based on the  $T_{mclath}$  data, using Diamond (1992). Bulk salinity varies from 0.5 to 1.7 wt% NaCl<sub>eq</sub>, and bulk

inclusion densities vary between 0.73 and 0.96 g/cm<sup>3</sup>. Overall, the narrow range of microthermometric properties of type 1a inclusions and their single-mode distribution suggest that the H<sub>2</sub>O–CO<sub>2</sub> ± CH<sub>4</sub>–NaCl<sub>eq</sub> fluid was trapped in the single-phase field and that trapping conditions did not vary systematically along the ARA strike.

Type 1b inclusions are primary inclusions of aqueous compositions, measured in eight BZ and WZ samples. This was the only type found in BZ apatite and quartz, but in WZ tourmaline, type 1b often coexisted with type 1a. Microthermometric properties of type 1b inclusions are widely variable. The homogenization temperatures vary from 195 to 351°C, with bimodal distribution (Fig. 5; Table 3). Generally, type 1b inclusions have lower  $T_h$  than the coexisting type 1a inclusions. An exception occurred in a single tourmaline sample from the WZ of northern ARA (325A2-a), where  $T_h$  of type 1b inclusions overlapped with and exceeded  $T_h$  of type 1a inclusions. Salinity of type 1b inclusions appears to vary with the mineral host and location within the pegmatite zones: highest salinities (19.8–20.2 wt% NaCl<sub>eq</sub>) in BZ apatite and the lowest salinities (0.3–1.0 wt% NaCl<sub>eq</sub>) in BZ quartz and WZ tourmaline (sample 325A2-a).

**Fig. 5** Center plot: salinity weight percentage (wt%) of NaCl equivalents versus temperature of homogenization  $T_h$  (°C). Left: salinity histograms. Right:  $T_h$  histograms. Fluid inclusion types: red 1a; green 1b inclusions; green open symbols 1b in BZ; orange 2a; violet type 2b. Mineral hosts: (open triangle) tourmaline; (open diamond) apatite; (open circle) quartz

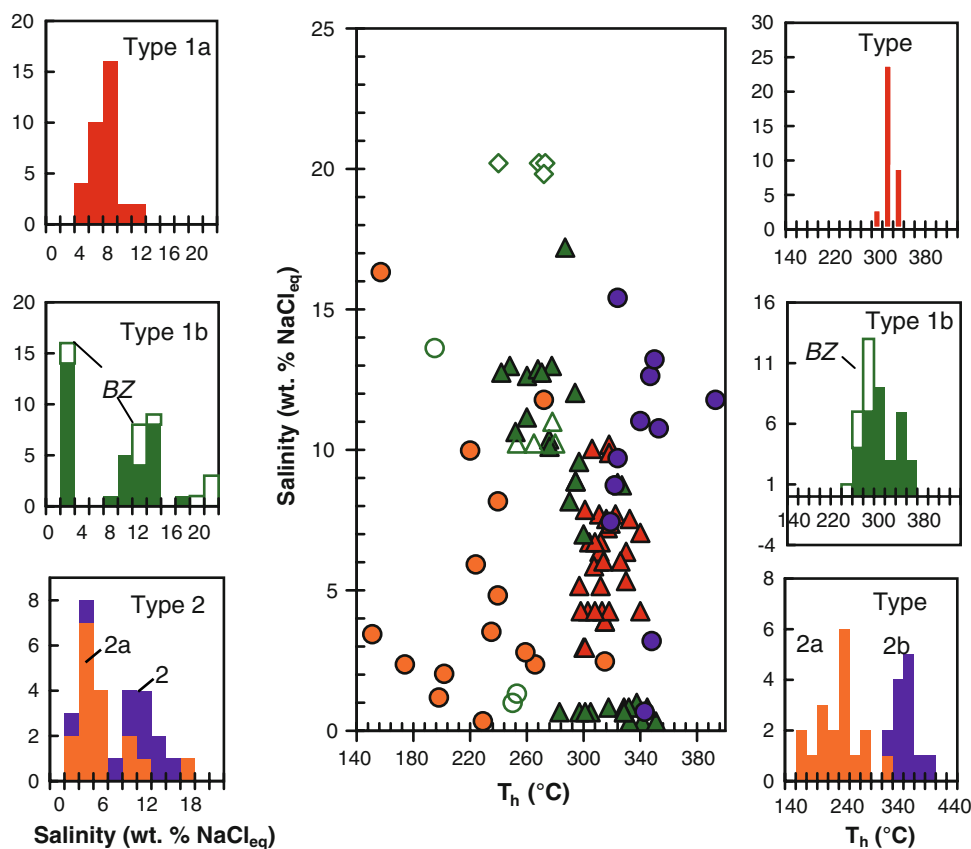


**Table 3** Summary of ARA fluid inclusion results

Sample					$T_h$ (°C)	Weight percentage (wt%) of $\text{NaCl}_{\text{eq}}^a$	$T_{\text{m,ice}}$ (°C)	$\rho$ (g/cm <sup>3</sup> )	
Locality	Number	Pegmatite zones	Host mineral	Inclus ion subtype					
ARA north	325A2-a	WZ HW	Pink <i>Tur</i>	<i>P, 1b</i>	283–351	0.3–1.0	–0.6 to –0.2	0.56–0.73	
	325G2	WZ	Pink <i>Tur</i>	<i>P, 1b</i>	290–327	8.2–9.6	–6.1 to –5.1	0.77–0.83	
ARA south	406A2	WZ, HW	Pink <i>Tur</i>	<i>P, 1b</i>	248–287	12.6–17.2	–12.8 to –8.5	0.89–0.92	
	406A2-a	WZ, HW	Pink/blue <i>Tur</i>	<i>P, 1b</i>	242–300	7.0–12.7	–8.6 to –4.3	0.79–0.93	
	406D-d	WZ, HW	Pink/blue, <i>Tur</i>	<i>P, 1b</i>	260–270	11.1–12.8	–8.6 to –7.6	0.89–0.90	
	406B2-a	CZ	20 cm from HW	Qtz	<i>PS/S, 2a</i>	157–272	0.3–16.3	–11.9 to –0.2	0.79–1.02
				Qtz	<i>PS/S, 2b</i>	224–393	0.7–15.4	–11 to –0.4	0.52–0.9
	406B2-b	CZ		Qtz	<i>PS/S, 2a</i>	151–315	2.5–4.6	–3.9 to –1.5	0.52–0.9
				Ap	<i>P, 1b</i>	240–273	19.8–20.2	–17 to –16.5	0.95–0.98
406A4-a	BZ, FW		<i>Tur</i>	<i>P, 1b</i>	253–280	10.2–11.0	–6.8 to –6.7	0.73–0.89	
			Qtz	<i>P, 1b?</i>	195–253	1.0–13.6	–0.6 to –9.7	0.80–0.97	
Mean $\pm$ standard deviation, number of inclusions				<i>P, 1b</i>	287 $\pm$ 34, 43	8.2 $\pm$ 6.4, 44	–5.7 $\pm$ 5.1, 43	0.80 $\pm$ 0.12, 44	
				<i>PS/S, 2a</i>	223 $\pm$ 45, 15	5.1 $\pm$ 4.5, 15	–3.3 $\pm$ 3.1, 16	0.85 $\pm$ 0.11, 16	
				<i>PS/S, 2b</i>	335 $\pm$ 34, 13	9.2 $\pm$ 4.3, 12	–6.0 $\pm$ 3.0, 12	0.74 $\pm$ 0.01, 13	

Primary, type 1b and secondary inclusions:  $\text{H}_2\text{O}$ – $\text{NaCl}_{\text{eq}}$  system

ARA north the northern segment of the dike, ARA south the southern segment of the dike, HW hanging wall, FW foot wall, BZ border zone, WZ wall zone, CZ core zone, *Tur* tourmalin, *Qtz* quartz, *Ap* apatite

Type 1b—primary (*P, 1b*) and types 2a and 2b—pseudosecondary/secondary (*PS/S, 2a,b*)

#### Pseudosecondary/secondary fluid inclusions in quartz (type 2)

One- or two-phase pseudosecondary/secondary inclusions distributed along <1 mm long healed fractures were analyzed in quartz only, because in other minerals they were too small or affected by necking. Twenty-nine inclusion results are reported from three samples from the WZ and CZ (Table 2). Type 2 inclusions are halite-undersaturated aqueous fluids of very low to moderate apparent salinity, with no detectable  $\text{CO}_2$  or other gases. Their size varies from <1 to 30  $\mu\text{m}$ , but most commonly in the 5–10  $\mu\text{m}$  range. Common inclusion shape is anhedral or ovoidal (Fig. 4d–f). Three subtypes were separated based on the degree of filling and/or association in distinct FIAs. Subtypes 2a and 2b occur along separate fractures and contain two fluid phases, with average degree of filling of 0.25 and 0.19, respectively. Subtype 2c are one-phase, liquid inclusions with last ice melting temperatures  $T_{\text{m,ice}}$  ranging from  $\sim -15^\circ\text{C}$  to  $-6^\circ\text{C}$  and do not nucleate a vapor bubble. They are omnipresent in quartz, occasionally along same trails as subtype 2a (Fig. 4d). We eliminated 2c inclusions from future discussion, because we could not determine their density and isochores. Salinities vary from 0.3 to 16.3 wt%  $\text{NaCl}_{\text{eq}}$  with mean values of 5.1 and 9.2 wt%  $\text{NaCl}_{\text{eq}}$  for types 2a and 2b, respectively (Table 3) based on freezing point depressions in the system  $\text{H}_2\text{O}$ – $\text{NaCl}$ – $\text{KCl}$ . Type 2a  $T_h$  values range from 151 to 315°C.

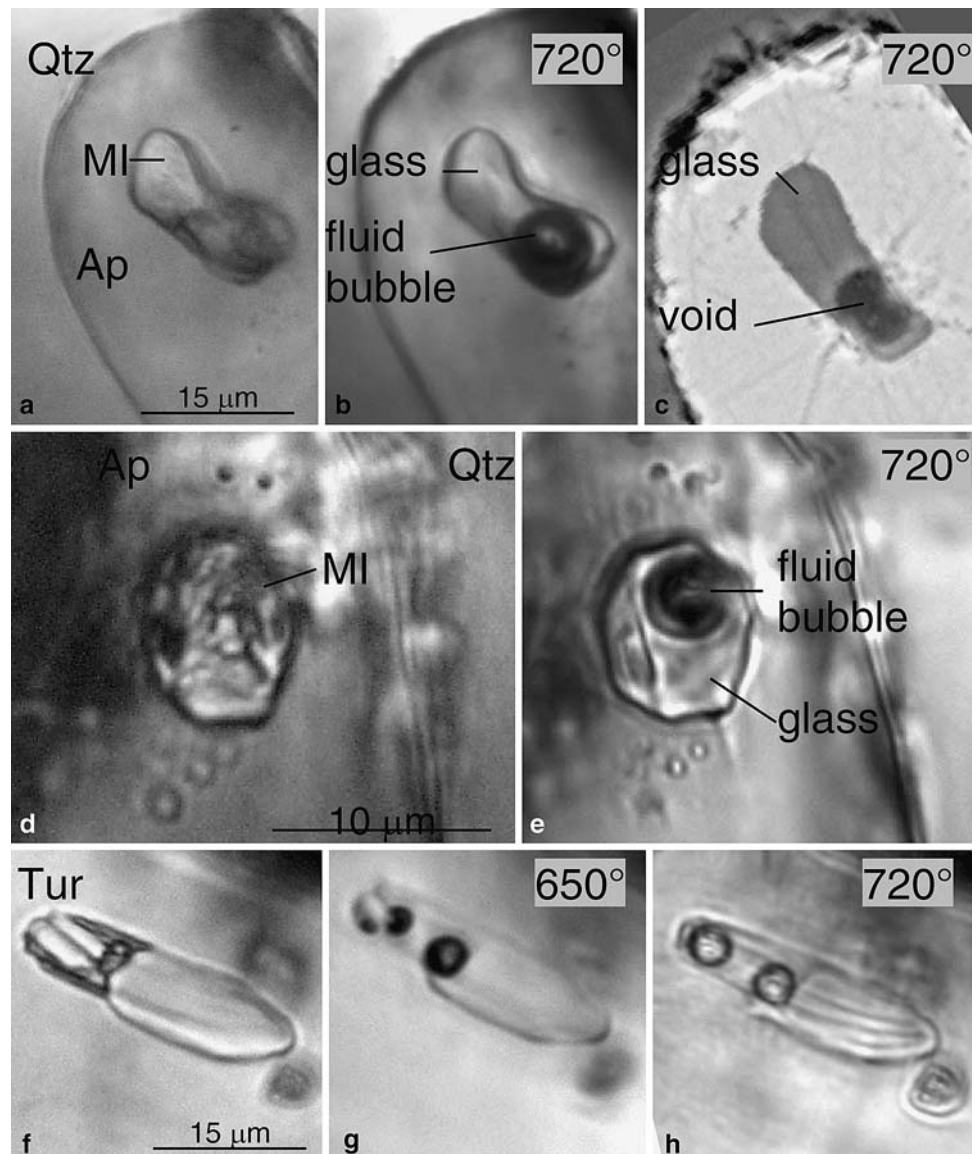
Type 2b  $T_h$  values are distinctively higher, ranging from 224 to 393°C. Densities (Table 3) and isochores were calculated using equations of state by Brown and Lamb (1989) and Zhang and Frantz (1987).

#### Crystallized-melt inclusions

About thirty-five crystallized-melt inclusions in apatite and five in tourmaline were documented before and after homogenization experiments. One-day long, stepwise heating runs performed in IHPVs followed by rapid quenching lead to complete melting of these inclusions to a homogeneous glass and  $\sim 20$ –30% fluid bubble at temperatures between 700 and 720°C and at 3–4 kbars (Fig. 6). This confirms that the crystal-rich inclusions in apatite and tourmaline were trapped melts. To date, we have not been able to observe the homogenization behavior of crystallized-melt inclusions in quartz.

Before remelting, the crystallized-melt inclusions contain  $\sim 20\%$  type 1 fluid and, from EDS-SEM observations, “daughter” grains of quartz, albite, K-feldspar, and muscovite (Fig. 6). The apparent volumetric ratios between phases were in general consistent, although infrequently, inclusions were dominated by one daughter mineral, were fluid-rich, or contained additional Cs-phases or columbite–tantallite group minerals. We interpret these inconsistencies as a result of accidental trapping of crystals or fluid bubbles

**Fig. 6** Crystallized-melt inclusions (*MI*) in BZ apatite (*Ap*) and tourmaline (*Tur*) at 25°C (**a**, **d**, and **f**) and after heating experiments at 4 kbars; all temperatures in °C; **c** backscatter electron image of inclusion from **a** and **b** exposed at surface by repolishing; melting of inclusion in **f** was incomplete at 650°C (**g**) and complete at 720°C (**h**)



in addition to melt. A relatively simple granitic composition of the trapped melt was confirmed by preliminary EMPA analysis of the homogenized inclusions exposed by sample repolishing.

All inclusions contained a fluid bubble after the heating experiments. We attribute the incomplete homogenization to bubble-free glass to instability of hydrous glass at these very high water concentrations, which may cause fluid nucleation during quenching of the runs. However, without complete homogenization of inclusions or a precise volumetric analysis to indicate constant proportions of fluid to glass, we cannot rule out that the melt and fluid were immiscible at 700–720°C (Student and Bodnar 1999), and that the inclusion trapping occurred heterogeneously.

### Fluid evolution

Assuming no post-trapping changes, the isochoric temperatures of fluid inclusions calculated for an independently derived trapping pressure should yield an estimate of the trapping temperature, i.e., (1) the temperature of crystallization of the host mineral if the inclusions are primary or (2) the temperature of fracture sealing if the inclusions are secondary or pseudosecondary (Roedder 1984). Inclusion isochores (Fig. 7) and isochoric temperatures (Fig. 8) were used to constrain the fluid evolution. We considered that internal fluid pressure was approximately the same as the lithostatic pressure of ~3 kbars, in agreement with data on hornblende geobarometry in the post-Penokean 1,760 granitoids (Holm 1998). Although the lithostatic pressure is

**Fig. 7** Fluid inclusion isochores and fluid stages at an emplacement pressure of 3 kbars. *Stage I* trapping of type 1a and 1b primary inclusions; *stage II* trapping of type 2b secondary inclusions and resetting of some 1b inclusions; *stage III* type 2a secondary fluids. Quartz-saturated Li–Al silicate diagram (London 1984): *Spd* spodumene, *Pet* petalite, *Vrg* virgilite, *Ecr* eucryptite; Al-silicates: *And* andalusite, *Sil* sillimanite, *Ky* kyanite

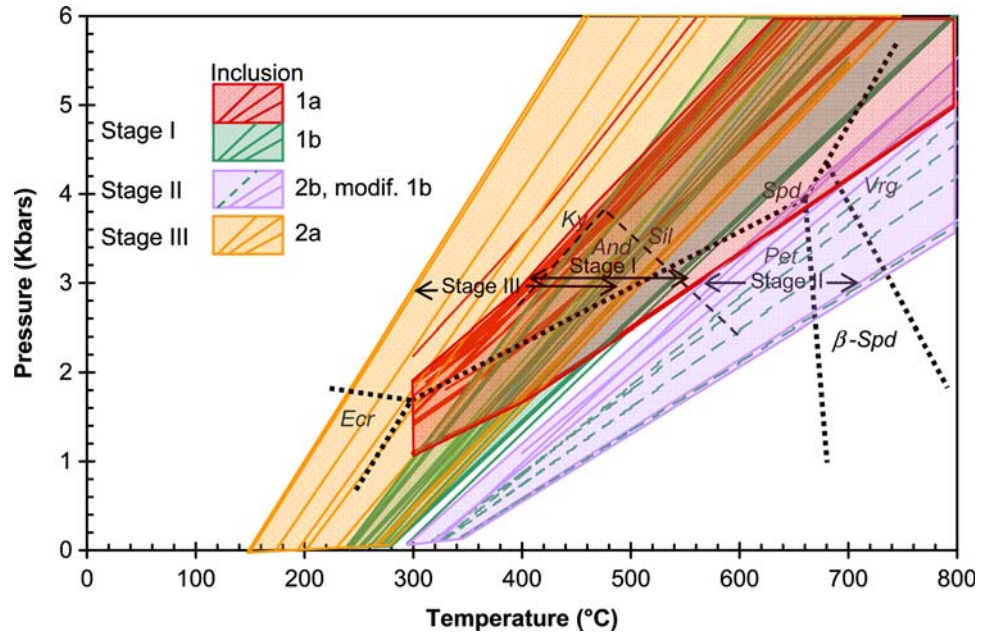
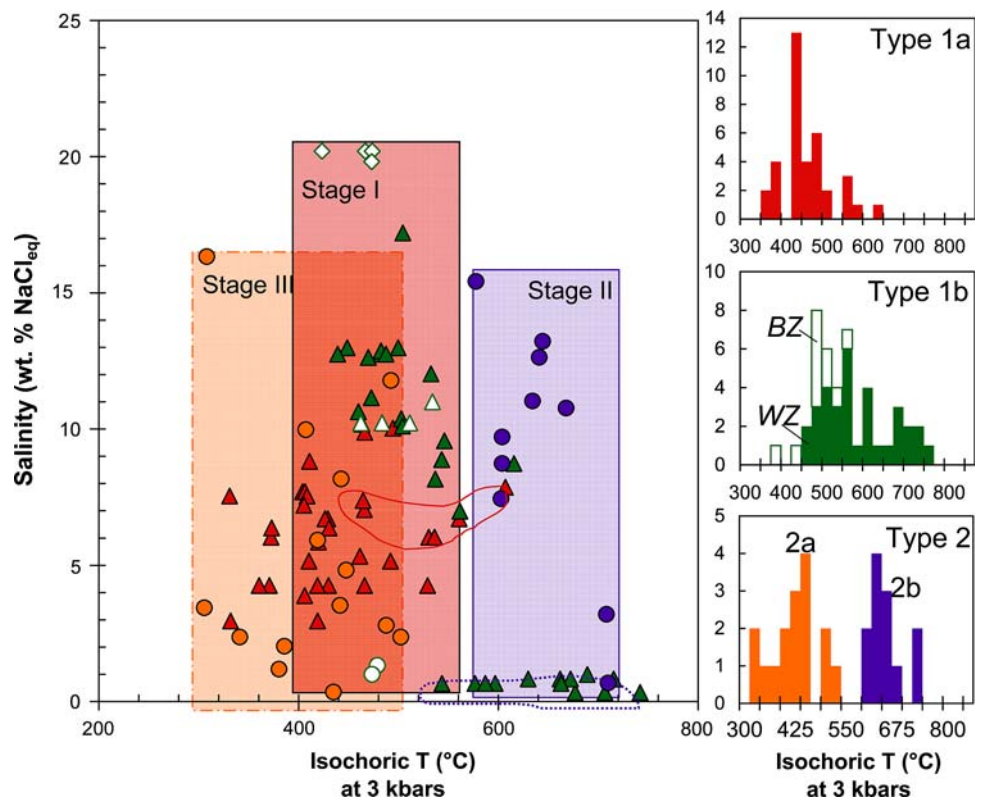


**Fig. 8** *Left*: salinity versus isochoric temperatures calculated for a pressure of 3 kbars; *Right*: isochoric temperature histograms. Symbols are the same as in Fig. 5. Fluid stages are the same as in Fig. 7. *Red crescent shape* outlines type 1a inclusions from late albite–aplite unit. *Violet dashed shape* outlines type 1b inclusions reset at high temperature



uncertain, the value of 3 kbars is constrained by stabilities of andalusite found in the metapelitic country rocks (Geiger and Guidotti 1989) and spodumene, the only Li–Al silicate described to date in ARA (Falster et al. 1996). The upper stability of andalusite of 3.75 kbars (Fig. 7) represents an upper limit of the lithostatic pressure, because the ARA

intrusion occurred post-tectonically, after significant uplift and cooling of the early Penokean andalusite-bearing schists, presumably formed at peak metamorphism. The stability field of spodumene constrains a minimum pressure ranging from 3.5 to 2.25 kbars, for temperature of crystallization of 600–400°C, respectively.

Assuming a pressure of  $\sim 3$  kbars, we separate three main stages of fluid trapping. Stage I comprises crystallization of the BZ mineral assemblage at temperatures ranging between 534 and 423°C based on unambiguously primary, type 1b inclusions, and of the WZ mineral assemblage between  $\sim 550$  and 410°C based on majority of type 1 inclusions in WZ tourmaline (Fig. 8). No systematic difference was found between crystallization temperatures of the hanging versus footwall WZ samples. Primary type 1a inclusions in blue tourmaline from a layered albite–aplite unit suggest that crystallization temperatures of inner zones range from 607 to 466°C, in part higher than the crystallization temperatures of the WZ assemblage (Figs. 7, 8).

At stage II, type 2b secondary inclusions were trapped at 580–720°C during deformation and fracturing of quartz, at the end of pegmatite crystallization, as hotter CZ and lepidolite and/or albite units crystallized. Therefore, the temperature of these secondary fluids was at least 170°C higher than the lowest crystallization temperature of the WZ tourmaline. The same late, high temperature processes may have reset some of the primary inclusions in WZ tourmaline (such as 325A2-a; Fig. 8).

At stage III, type 2a secondary inclusions (Figs. 7, 8) were trapped in fractured quartz from all zones at variable temperatures as low as  $\sim 300^\circ\text{C}$ , most likely at subsolidus conditions. Given the overlap of isochoric temperatures and salinities of types 1 and 2a inclusions, it is conceivable that many of the 2a inclusions in quartz were also trapped at stage I, but texturally we were not able to unambiguously identify primary or pseudosecondary type 2a FIAs.

The ARA magmatic fluid was trapped either as mixtures of  $\text{H}_2\text{O}$ – $\text{CO}_2$  (type 1a inclusions) or aqueous fluids with no  $\text{CO}_2$  (all other types), included in variable proportions by different minerals. For instance, WZ tourmaline included  $\sim 80\%$   $\text{H}_2\text{O}$ – $\text{CO}_2$  and 20% aqueous fluid (often coexisting in the same crystal), while apatite and quartz included only aqueous fluid. Both compositional fluid types appear through the entire sequence of crystallization, from the outer zones to the late crosscutting units. All inclusions homogenized to a liquid phase, regardless of their composition, which discards the possibility of trapping under fluid immiscibility conditions.

It is difficult to conceive that all type 1b inclusions originated as type 1a and subsequently lost  $\text{CO}_2$  because of some late resetting process. Massive  $\text{CO}_2$  release from these inclusions would manifest as  $\text{CO}_2$ -rich secondary inclusions or secondary carbonates in the surrounding minerals, but none of these have been found. Instead, the composition of the fluid exsolved from the crystallizing magma and trapped at the crystal–magma interface may have been affected by rapid, disequilibrium crystallization. As such, the variable inclusion chemistry may be due to

different diffusivities of  $\text{H}_2\text{O}$  and  $\text{CO}_2$  in the rapidly advancing crystallization front and their different surface tension in various host minerals. However, the trapping  $P$ – $T$  conditions should be correctly portrayed by fluid inclusion density, a physical parameter not influenced by disequilibrium crystallization.

### Numerical cooling simulations

We used the finite differencing computer code Kware HEAT3D, version 4 (Wohletz et al. 1999) to simulate the conductive cooling of the ARA magma body and to estimate the spatial and temporal temperature profiles within the pegmatite body and country rock. Pertinent variables were selected based on field constraints and optimized to test the crystallization conditions inferred from microthermometry. We considered an instantaneous, single injection of 2.5 m thick, “infinite” horizontal sheet of nonconvective 720°C felsic magma with a thermal conductivity of  $1.1 \text{ W m}^{-1} \text{ K}^{-1}$ , heat capacity of  $1,100 \text{ J kg}^{-1} \text{ K}^{-1}$ , and a density of  $2,250 \text{ kg/m}^3$ , intruding a nonporous metamorphic rock with a thermal conductivity of  $3.5 \text{ W m}^{-1} \text{ K}^{-1}$ , heat capacity of  $980 \text{ J kg}^{-1} \text{ K}^{-1}$ , and a density of  $2,800 \text{ kg/m}^3$  to approximate the nonporous quartz-rich schist of the country rock (Robertson 1988; Clauser and Huenges 1995). The pressure–temperature dependencies of Chapman and Furlong (1992) for thermal conductivity are imbedded in the HEAT3D program. The depth of about 11 km was selected to simulate a lithostatic pressure of 3 kbars. For this depth, the geothermal gradient of  $20^\circ\text{C/km}$ , starting with  $0^\circ\text{C}$  temperature at the surface, led to a temperature of the country rocks of  $220^\circ\text{C}$ . The computational mesh was  $20 \times 20 \times 20 \text{ m}^3$  with a grid unit of 0.1 m. The computational time step was 0.005 days.

Two different computational sets were explored, with or without latent heat of crystallization generated by the magma. Data were collected at 0.1-day intervals for the first day, then at 1-day intervals, to a total of 70 days. Isotherms and vertical temperature profiles (Figs. 9, 10) were calculated as a function of time. When cooling was allowed to proceed without latent heat of crystallization, the simulation reproduced successfully the  $\geq 170^\circ\text{C}$  temperature contrast suggested by fluid inclusion results, between fluids released from the pegmatite core and the already crystallized pegmatite margins (Fig. 10). The temperature of the magma within 10 cm from the contact drops to  $455^\circ\text{C}$  at  $t = 0.5$  days, to  $430^\circ\text{C}$  at  $t = 2$  days, and then it cools slowly to  $410^\circ\text{C}$  at  $t = 14$  days (Fig. 10). In contrast, in the core of the pegmatite, there is no significant magma cooling for the first 2 days, after which the core starts cooling at a faster rate than the margin down to  $\sim 580^\circ\text{C}$  at  $t = 14$  days (Fig. 10). Introduction of latent

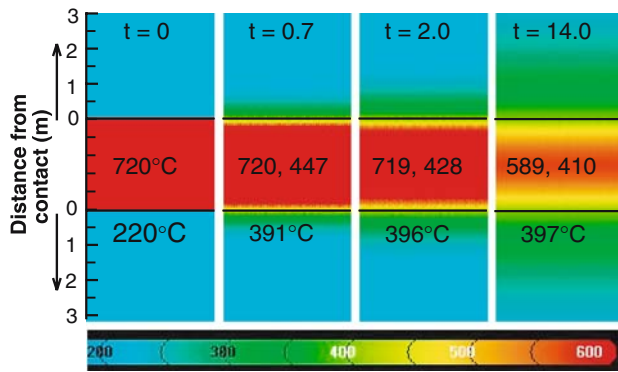


**Fig. 9** HEAT3D vertical profiles of the ARA pegmatite at time  $t = 0, 0.7, 2,$  and  $14$  days after instantaneous intrusion of a  $2.5\text{-m}$ -thick horizontal magma sheet in nonporous metamorphic rock at a depth of  $\sim 11$  km. Temperature maxima and minima are shown for the pegmatite and maxima for the country rock in  $^{\circ}\text{C}$  (see text for input parameters)

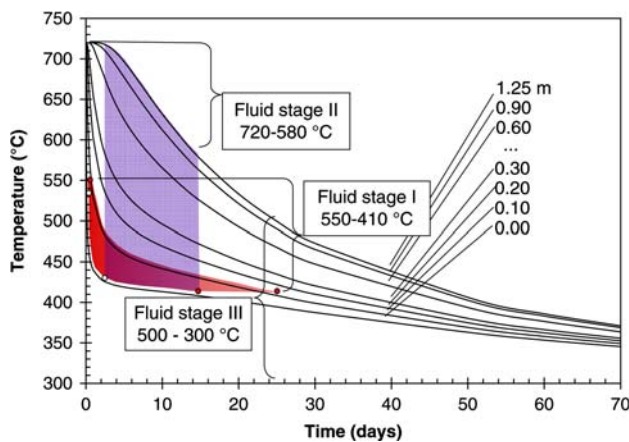


**Fig. 10** Simulated temperature–time cooling profiles for watch points at variable distances from the contact. Fluid stages I, II, and III are labeled within boxes using curly brackets. The BZ and WZ maximum and minimum trapping temperatures and inferred WZ crystallization ranges are shown in white and red circles, and a red field, respectively. The secondary fluid generated from the crystallizing core at stage II and overlapping onto inner zones is shown as a violet field

heat of crystallization slowed down the cooling, in which case the ARA margins reached the solidification temperature of  $410^{\circ}\text{C}$  at  $\sim 32$  days. At this time, the temperature of the core would be only  $485^{\circ}\text{C}$ , which would be insufficient to explain the high temperature secondary inclusions (type 2b).

### Petrogenetic model and discussion

Based on field observations, the ARA thin dike was emplaced mostly discordantly in fractured country rocks, at

$10\text{--}11$  km depth, assuming that it is related to the  $1,760$  Ma post-Penokean magmatism (Holm et al. 2005). The pressure of emplacement of  $\sim 3$  kbars is an important assumption in this model, because all trapping temperatures inferred from fluid inclusions are isochoric temperatures, calculated as a function of pressure (Fig. 8). However, if the emplacement pressures were to be different, the crystallization scenario exposed below would not change, only the absolute temperatures change. Regardless of pressure, the liquidus temperature was  $\sim 720^{\circ}\text{C}$ , as suggested by equilibrium melting of the MIs from the chilled margin BZ.

The cooling rate of the pegmatite margins averaged  $22^{\circ}\text{C}/\text{h}$  in the first 12 h,  $1.3^{\circ}\text{C}/\text{h}$  for the next 12 h, and  $\sim 0.1^{\circ}\text{C}/\text{h}$  for the next 13 days (Fig. 10). In the BZ, this extremely fast cooling suppressed crystal nucleation until the melt reached  $\sim 530^{\circ}\text{C}$  at most, the highest trapping temperature recorded in tourmaline. The  $<3$  mm chilled margin assemblage of the BZ developed at  $478 \pm 30^{\circ}\text{C}$ , with a high nucleation rate (Fig. 3b, c) perhaps enhanced by mineral–fluid reactions at the contact with the country rock. However, this first pulse of crystallization produced an insignificant volume of the dike. Crystallization of WZ (first 10 cm or  $\sim 10\%$  of the pegmatite) occurred between  $\sim 550^{\circ}\text{C}$  (starting at  $t = 0.1\text{--}0.7$  days) and  $410^{\circ}\text{C}$  (at  $t = 14\text{--}25$  days), as indicated by the trapping temperatures of 83% of type 1 inclusions (Fig. 8). Within analytical error, there is no systematical temperature variation within the thickness of the WZ or along the strike.

According to inclusion microthermometry and numerical simulations, crystallization of the ARA was triggered at an undercooling value of  $\sim 240^{\circ}\text{C}$  in the BZ and at least at  $\sim 170^{\circ}\text{C}$  in the WZ. Only simulations excluding internal heat of crystallization reproduced the microthermometric data. This is consistent with the ARA persistence as an undercooled liquid down to as little as  $410^{\circ}\text{C}$  in its margins. Rapid, disequilibrium crystallization was previously inferred from presence of intermediate microcline and complex compositional zoning of columbite–tantallite (Falster et al. 1996). Crystallization in undercooled state is also indicated by comb textures, unidirectional or radial aggregates, skeletal intergrowths (Fig. 3e–h), and inclusion-loaded crystals in the marginal zones (Fig. 4b). Alternating tourmaline–apatite-rich and poor zones and rhythmic textural variations in the lepidolite pods are also suggestive of diffusion-controlled, very rapid crystallization.

Type 2b secondary inclusions were trapped at temperatures ranging from  $\sim 720$  to  $580^{\circ}\text{C}$ , higher than the margins that formed between  $\sim 550$  and  $410^{\circ}\text{C}$ . In a simple, single-injection scenario, these hotter melts and fluids could have been released from the crystallizing inner zones. According to the HEAT3D model, the temperature difference of  $\geq 170^{\circ}\text{C}$  between the ARA core and

margin lasted up to  $t = 14$  days (Fig. 10). The hotter fluid overprint is associated with mineral replacement textures (Fig. 3i) and late crosscutting magmatic units (Fig. 3j, k). In addition, comb and skeletal textures in the late crosscutting units (Fig. 3h, j, k) indicate that, indeed, melt from the core injected the crystalline, colder outer zones. Therefore, based on microthermometric, modeling, and textural premises, crystallization of the core and derived crosscutting units was triggered after, but overlapped in part with, the crystallization of the ARA margins (Fig. 11).

The model also simulates a rapid and short-lived temperature increase in the country rock at the contact with the

ARA melt, preventing extensive metasomatism of the country rock. Fluid flow through essentially impermeable country rock would not keep up with the thermal anomaly. Textural relationships in the schist within the first few centimeters from the contact suggest that, although very limited, some mass transfer occurred at the contact with the rapidly crystallizing melt. Tourmalinization in areas of discordant contacts occurred just before or simultaneously with BZ tourmaline growth (Fig. 3b); thus, the replacement reactions had to occur very fast and the magma was already fluid-saturated. Although the overall porosity of the schist is thought to be very low, foliation-parallel permeability may have enhanced fluid transport in areas of discordant contacts.

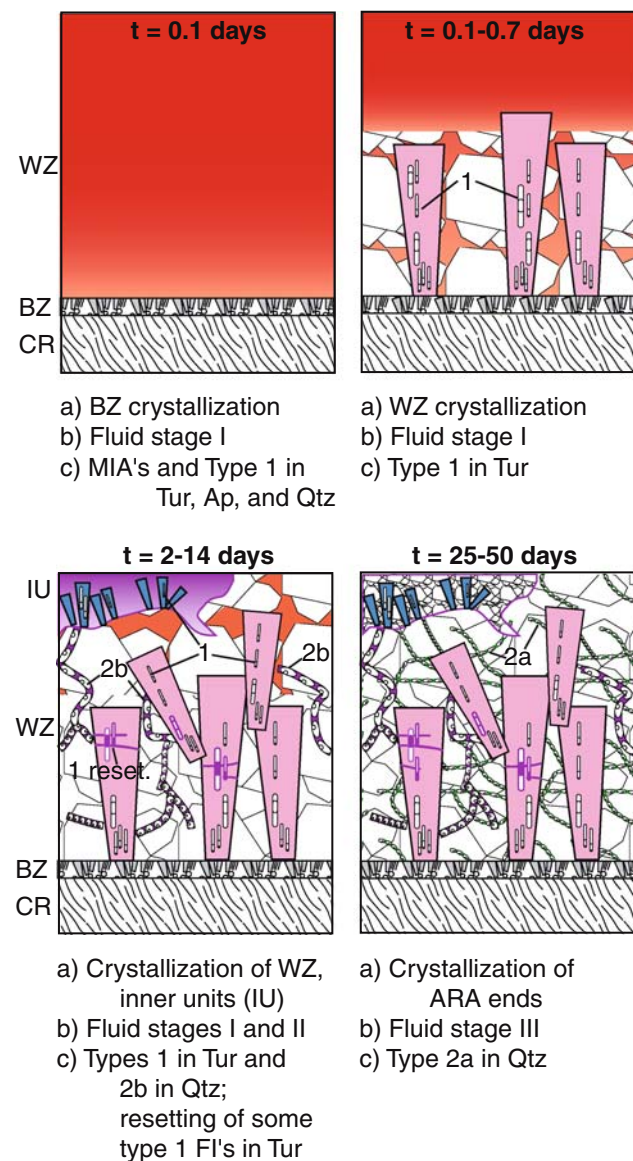


**Fig. 11** Four intervals of ARA crystallization and fluid evolution. Items described for each interval: *a* units crystallizing; *b* fluid stages; *c* inclusion types and their mineral host

## Conclusions

Coeval MIAs and FIAs were used to determine the degree of magma undercooling at the onset of crystallization. The MI homogenization temperatures constrained via stepwise experiments in IHPVs approach equilibrium melting; therefore, they provide an estimate of the liquidus temperature of the melt. The pressure-corrected homogenization temperatures of primary FIAs provide an estimate of the temperature at which the host crystals actually formed. This method can be applied to understanding disequilibrium crystallization of magma of other compositions, providing that coeval primary MIAs and FIAs can be documented and the undercooling is large enough relative to the analytical errors.

This study documents secondary FIAs trapped at temperatures higher than coexisting primary FIAs. We have shown that rapid cooling of a magma sheet singly injected in colder rocks promoted this telescopic overlap. The ARA crystallized sequentially, from the outer to the inner zones; however, based on combined inclusion results and HEAT3D modeling, there was a significant overlap. Coupling inclusion work with high-resolution thermal modeling may be used to explain multiple fluid inclusion generations and their parental magmatic processes and can potentially be applied to various petrological and ore deposits problems.

Li, B, and Cs minerals such as elbaite and rhodizite found in the WZ suggest high complexity of the ARA initial melt. The high amounts of fluxing and depolymerizing components contributed to the very low temperature of crystallization by depressing the glass transition, and thus allowing the ARA persistence as an undercooled liquid down to temperatures as low as 400°C.

**Acknowledgments** We thank Dave Jenkins, Bill Blackburn, and Tim Lowenstein at Binghamton University for support with

hydrothermal experiments, EMPA analysis, and use of the microscopy lab. Phil Oshel at Central Michigan University (CMU) assisted with the SEM analyses. Two CMU Office of Research and Sponsored Programs grants to Sirbescu and undergraduate student Hartwick supported this project. Al Falster and the Wisconsin Department of Natural Resources are thanked for information about how to access and releasing access to the ARA pegmatite, respectively. The manuscript benefited from thoughtful comments and remarks from Jacques Touret and from thorough suggestions by an anonymous reviewer.

## References

- Bayley RW, Dutton CE, Lamey CA, Treves SB (1966) Geology of the Menominee iron-bearing district, Dickinson County, Michigan, and Florence and Marinette counties, Wisconsin (US Geological Survey Professional Paper 513). US Geological Survey, Reston, VA, p 96
- Bodnar RJ, Student JJ (2006) Melt inclusions in plutonic rocks: petrography and microthermometry. In: Webster JD (ed) Melt inclusions in plutonic rocks, vol 36. Mineralogical Association of Canada, Quebec, pp 1–25
- Bouhifd MA, Whittington ARJ, Roux J, Richet P (2006) Effect of water on the heat capacity of polymerized aluminosilicate glasses and melts. *Geochim Cosmochim Acta* 70:711–722
- Brown PE, Hagemann SG (1995) MacFlinCor and its application to fluids in Archean lode-gold deposits. *Geochim Cosmochim Acta* 59:3943–3952
- Brown PE, Lamb WM (1989) P–V–T–X properties of fluids in the system  $H_2O$ – $CO_2$ –NaCl: new graphical presentations and implications for fluid inclusion studies. *Geochim Cosmochim Acta* 53:1209–1221
- Cameron EM, Jahns RH, McNair AH, Page LR (1949) Internal structure of granitic pegmatites. *Economic Geology Monograph* 2, p 115
- Černý P (1993a) Rare-element granitic pegmatites. Part I: anatomy and internal evolution of pegmatite deposits. In: Sheahan PA, Cherry ME (eds) Ore deposit models (Geoscience Canada reprint series, vol 6). Geological Association of Canada, St. John's, Newfoundland, pp 29–47
- Černý P (1993b) Rare-element granitic pegmatites. Part II: regional to global environments and petrogenesis. In: Sheahan PA, Cherry ME (eds) Ore deposit models (Geoscience Canada reprint series, vol 6). Geological Association of Canada, St. John's, Newfoundland, pp 49–62
- Černý P, Ercit S (2005) The classification of granitic pegmatites revisited. *Can Mineral* 43:2005–2026
- Černý P, Blevin PL, Cuney M, London D (2005) Granite-related ore deposits. In: Hedenquist J, Thompson JFH, Goldfarb RJ, Richards JP (eds) Economic geology 100th anniversary volume. Society of Economic Geologists, Littleton, pp 337–370
- Chapman DS, Furlong KP (1992) Thermal state of the continental crust. In: Fountain DM, Arculus RJ, Kay RW (eds) Continental Lower Crust, vol. 23. Elsevier, New York, pp 179–199
- Clauser C, Huenges E (1995) Thermal conductivity of rocks and minerals. In: Ahrens TJ (ed) Rock physics and phase relations—a handbook of physical constants, AGU reference shelf, vol 3. American Geophysical Union, Washington, DC, pp 105–126
- Diamond LW (1992) Stability of  $CO_2$  clathrate hydrate +  $CO_2$  liquid +  $CO_2$  vapour + aqueous KCl–NaCl solutions: experimental determination and application to salinity estimates of fluid inclusions. *Geochim Cosmochim Acta* 56:273–280
- Dutton CE (1971) Geology of the Florence area, Wisconsin and Michigan. Scale 1:24,000 (US Geological Survey Professional Paper 633). US Geological Survey, Reston, VA, p 54
- Ercit TS, Groat LA, Gault RA (2003) Granitic pegmatites of the O'Grady batholith, N.W.T., Canada: a case study of the evolution of the elbaite subtype of rare-element granitic pegmatite. *Can Mineral* 41:117–137
- Falster AU, Simmons WB (1988) Emplacement, mineralogy, and internal evolution of a highly evolved Li-pegmatite in Florence county, Wisconsin. In: Klasner JS, Hughes JD, Schultz KJ (eds) 34th annual meeting, Institute on Lake Superior Geology proceedings (Marquette, MI, 12–13 May 1988), Part 1, Abstracts, vol 34. Institute on Lake Superior Geology, pp 26–28
- Falster AU, Simmons WB, Webber KL (1996) The mineralogy and geochemistry of the Animikie Red Ace pegmatite, Florence county, Wisconsin. *Rec Res Dev Mineral* 1:7–67
- Falster AU, Simmons WB, Webber KL (2005) Origin of the pegmatites in the Hoskin Lake pegmatite field, Florence county, Wisconsin. In: Pezzotta F (ed) Crystallization Processes in granitic pegmatites, international meeting, Mineralogical Society of America, Cavoli, Elba Island, Italy. [http://www.minsocam.org/msa/special/Pig/PIG\\_articles/PIG\\_articles.html](http://www.minsocam.org/msa/special/Pig/PIG_articles/PIG_articles.html)
- Falster AU, Simmons WB, Webber KL (1997) Unusual chemistry of tourmaline in the Animikie Red Ace Pegmatite in Florence county, Wisconsin, U.S.A. In: Tourmaline 1997; international symposium on Tourmaline, Czech Republic Ministry of Education
- Falster AU, Simmons WB, Webber KL (2001) Unorthodox compositional trends in columbite-group minerals from the Animikie Red Ace Pegmatite, Wisconsin, USA. *J Czech Geol Soc* 46:69–79
- Geiger CA, Guidotti CV (1989) Precambrian metamorphism in the southern Lake Superior region and its bearing on crustal evolution. *Geoscience Wisconsin* 13:1–33
- Goldstein RH, Reynolds TJ (1994) Systematics of fluid inclusions in diagenetic minerals, short course notes 31. SEPM (Society for Sedimentary Geology), Tulsa, OK, p 199
- Hoffman PF (1989) Precambrian geology and tectonic history of North America. In: Bally AW, Palmer AR (eds) The geology of North America—an overview, vol A. Geological Society of America, Boulder, CO, pp 447–512
- Holm DK (1998) From accretion to cratonization; new insights from the post-Penokean (1800–1400 Ma) tectonic evolution of the North American midcontinent. In: Anonymous (ed) 14th International Conference on Basement Tectonics, Blacksburg, Virginia, June 1998, 14:104–106
- Holm DK, Van Schmus WR, MacNeill LC, Boerboom TJ, Schweitzer D, Schneider D (2005) U–Pb zircon geochronology of Paleoproterozoic plutons from the northern midcontinent, USA: evidence for subduction flip and continued convergence after Geon 18 Penokean orogenesis. *Geol Soc Am Bull* 117:259–275
- Jenkins DM, Clare AK (1990) Comparison of the high-temperature and high-pressure stability limits of synthetic and natural tremolite. *Am Mineral* 75:358–366
- Koehler SR (1990) Geological setting and geochemistry of the Bush Lake Granite in relation to rare-element pegmatites, Florence county, Wisconsin. In: Fralick PW (ed) Institute on Lake Superior Geology, 36th annual meeting, vol 36. Institute on Lake Superior Geology, p 51
- London D (1984) Experimental phase equilibria in the system  $LiAlSiO_4$ – $Si_2O$ – $H_2O$ : a petrogenetic grid for lithium-rich pegmatites. *Am Mineral* 69:995–1004
- London D (2005) Granitic pegmatites: an assessment of current concepts and directions for the future. *Lithos* 2005:281–303
- Luth WC, Jahns RH, Tuttle OF (1964) The granite system at pressures of 4 to 10 kilobars. *J Geophys Res* 69:759–773
- Marshall DD, Groat LA, Falck H, Giuliani G, Neufeld H (2004) The Lened emerald prospect, Northwest Territories, Canada: insights from fluid inclusions and stable isotopes, with implications for Northern Cordilleran emerald. *Can Mineral* 42:1523–1539



- Morgan GBV, London D (1999) Crystallization of the Little Three layered pegmatite-aplite dike, Ramona District, California. *Contrib Mineral Petrol* 136:310–330
- Nabelek PI, Sirbescu M-LC (2006) A kinetic model for crystallization of very low temperature pegmatitic melts. *Eos transactions of the American Geophysical Union* 87, Joint Assembly Supplement, Abstract V53A-02
- Robertson EC (1988) Thermal properties of rocks. US Geological Survey open file report 88-441, p 106
- Roedder E (1984) Fluid inclusions. In: Ribbe PH (eds) *Reviews of mineralogy*, vol 12. Mineralogical Society of America, Washington, DC, p 646
- Schneider DA, Bickford ME, Cannon WF, Schulz KJ, Hamilton MA (2002) Age of volcanic rocks and syndepositional iron formations, Marquette range supergroup: implications for the tectonic setting of paleoproterozoic iron formations of the Lake Superior region. *Can J Earth Sci* 39:999–1012
- Shepherd TJ, Rankin AH, Alderton DHM (1985) A practical guide to fluid inclusions studies. Blackie, Glasgow, p 239
- Sims PK, Peterman ZE, Schulz KJ (1985) Dunbar gneiss-granitoid dome: implications for Proterozoic tectonic evolution of northern Wisconsin. *Geol Soc Am Bull* 96:1101–1112
- Sims PK, Schulz KJ, Peterman ZE (1992) Geology and geochemistry of early proterozoic rocks in the Dunbar area, northeastern Wisconsin (US Geological Survey Professional Paper 1517). US Geological Survey, Reston, VA, p 65
- Sims PK, Van Schmus W (1988) Geologic map of the Dunbar and Dunbar NE quadrangles. In: U.S. Geological Survey miscellaneous investigations series map, vol I-1714, scale 1:24,000. US Geological Survey, Reston, VA
- Sirbescu M-LC, Nabelek PI (2003) Crustal melts below 400°C. *Geology* 31:685–688
- Smirnov SZ, Thomas VG, Demin SP, Drebushchak VA (2005) Experimental study of boron solubility and speciation in the Na<sub>2</sub>O–B<sub>2</sub>O<sub>3</sub>–SiO<sub>2</sub>–H<sub>2</sub>O system. *Chem Geol* 223:16–34
- Student JJ, Bodnar RJ (1999) Synthetic fluid inclusions XIV: coexisting silicate melt and aqueous fluid inclusions in the haplogranite–H<sub>2</sub>O–NaCl–KCl system. *J Petrol* 40:1509–1525
- Thiery R, Van Den Kerkhof AM, Dubessy J (1994) VX properties of CH<sub>4</sub>–CO<sub>2</sub> and CO<sub>2</sub>–N<sub>2</sub> fluid inclusions: modelling for  $T < 31^{\circ}\text{C}$  and  $P < 400$  bars. *Eur J Mineral* 6:753–771
- Thomas R, Webster JD, Heinrich W (2000) Melt inclusions in pegmatite quartz: complete miscibility between silicate melts and hydrous fluids at low pressure. *Contrib Mineral Petrol* 139:394–401
- Thomas R, Foerster H-J, Rickers K, Webster JD (2005) Formation of extremely F-rich hydrous melt fractions and hydrothermal fluids during differentiation of highly evolved tin-granite magmas; a melt-fluid-inclusion study. *Contrib Mineral Petrol* 148:582–601
- Touret JLR, Smirnov SZ, Thomas VG, Peretyazhko IS, Zagorsky VYe (2007) Magmatic/hydrothermal transition in tourmaline-bearing miarolitic pegmatites: hydrosaline fluids or silica gels? In: *Granitic pegmatites: the state of the art—international symposium*, Porto, Portugal, abstract 2p
- Van Schmus WR (1976) Early and middle Proterozoic history of the Great Lakes area, North America. *R Soc Lond Philos Trans* 280:605–628
- Veksler IV, Thomas R (2002) An experimental study of B-, P- and F-rich synthetic granite pegmatite at 0.1 and 0.2 GPa. *Contrib Mineral Petrol* 143:673–683
- Webber KL, Simmons WB, Falster AU, Foord EE (1999) Cooling rates and crystallization dynamics of shallow level pegmatite-aplite dikes, San Diego County, California. *Am Mineral* 84:708–717
- Wohletz K, Civetta L, Orsi G (1999) Thermal evolution of the Phlegraean magmatic system. *Volcanism in the Campi Flegrei*. *J Volc Geotherm Res* 91:381–414
- Zhang Y-G, Frantz JD (1987) Determination of the homogenization temperatures and densities of supercritical fluids in the system NaCl–KCl–CaCl<sub>2</sub>–H<sub>2</sub>O using synthetic fluid inclusions. *Chem Geol* 64:335–350